Supplementary Information

CO_2 Electroreduction to CO over Silver Nanoclusters: The Impact of Nuclearity on Synergistic Activity Modulation

Parvathy Jayan[1#], Arijit Jana[2#], Zhengyuan Li[3], Rahul Kumar Sharma[4], Vivek Yadav[2],Astrid Campos Mata[5], Ming-Husan Li[6], Ali Shayesteh Zeraati[7], Tomas Base[8], Sung-Fu Hung[6], Jingjie Wu[3], Biswarup Pathak[4], Thalappil Pradeep[2], Soumyabrata Roy*[1,5]

[1]Department of Sustainable Energy Engineering, Indian Institute of Technology Kanpur, Uttar Pradesh, India

[2]Department of Science and Technology (DST) Unit of Nanoscience and Thematic Unit of Excellence, Department of Chemistry, Indian Institute of Technology (IIT) Madras, Chennai, India

[3]Department of Chemical Engineering, University of Cincinnati, Cincinnati, OH 45221, USA

[4]Department of Chemistry, Indian Institute of Technology, Indore, Madhya Pradesh. India

[5]Department of Materials Science and Nanoengineering, Rice University, Houston, Texas 77005, USA

[6]Department of Applied Chemistry and Centre for Emergent Functional Matter Science, National Yang Ming Chiao Tung University, Hsinchu 300, Taiwan.

[7]Acceleration Consortium, University of Toronto, 80 St. George St., Toronto, ON M5S 3H6, Canada

[8]Department of Syntheses, Institute of Inorganic Chemistry, The Czech Academy of Sciences, 1001 Husinec-Rez, 25068, Czech Republic.

[#] These authors contributed equally: Parvathy Jayan, Arijit Jana

Email: soumyar@iitk.ac.in (Soumyabrata Roy)

Index

1. **Instrumental details and characterization** S4
2. **Computational Detail** S5
3. **Figures**

Figure S1. SEM-EDS images of Ag_{21} NC and EDS spectra S6

Figure S2. Photographic images of UV-visible samples of AgNCs in cuvettes S6

Figure S3. UV-vis absorption spectra of (a) Ag_{22}, (b) Ag_{44} before loading the GDL S6

Figure S4. HR-MS spectra of Ag_{22} and Ag_{44} NCs S7

Figure S5. Single-crystal images of Ag_{21} NC and Ag_{42} NC S7

Figure S6. TEM image of Ag NCs S8

Figure S7. HAADF elemental mapping of Ag_{21} NC S8

Figure S8. FTIR Spectra of Ag_{31} and Ag_{42} S9

Figure S9. HR-Elemental XPS scans and peak fitting of Ag_{21} NC catalysts S9

Figure S10. HR-Elemental XPS scans and peak fitting of Ag_{31} NC catalysts S10

Figure S11. HR-Elemental XPS scans and peak fitting of Ag_{42} NC catalysts S10

Figure S12. Faradaic Efficiency (FE) of CO for Ag_{31}NC and Ag_{42} NC S11

Figure S13. Electrochemical performance of Ag_{22} in comparison with Ag_{21} S11

Figure S14. Electrochemical performance of Ag_{42} in comparison with Ag_{44} S12

Figure S15. Long-term stability data of Ag_{21} S12

Figure S16. Pre- and post-electrochemical XPS peak fitting of Ag_{21}NC catalyst-coated electrode. S13

Figure S17. Pre- and post-electrochemical XPS peak fitting of Ag_{31}NC catalyst-coated electrode. S13

Figure S18. Pre- and post-electrochemical XPS peak fitting of Ag_{42}NC catalyst-coated electrode. S14

Figure S19. EXAFS spectra of Ag K edge for the AgNCs post eCO_2R S14

Figure S20. EXAFS fitting result of AgNCs at R space after eCO_2R S15

Figure S21. Heterogeneous Active Sites Investigated for *CO and *COOH adsorption on the Ag_{21} cluster. S15

Figure S22. Heterogeneous Active Sites Investigated for *CO and *COOH adsorption on the Ag_{42} cluster. S16

Figure S23. CDD plots on intermediate *COOH and CO on Ag_{21} and Ag_{42} S16

Figure S24. Heterogeneous Active Sites Investigated for *CO, and *COOH adsorption on the Ag_{44} cluster S17

Figure S25. Gibbs free energy diagram of Ag_{21}, Ag_{42}, and Ag_{44} clusters S17

Figure S26. Total and partial DOS analysis for *COOH and *CO-adsorbed Ag_{21} and Ag_{42} clusters S18

Figure S27. Subplots for total and partial density of states (DOS) for *COOH, and *CO-adsorbed on Ag_{42}. S28

Figure S28. Subplots for total and partial density of states (DOS) for *COOH, and *CO-adsorbed on Ag_{21}. S19

4. Tables

Table S1. EXAFS fitting parameters of Ag NC catalyst S19

Table S2. Comparison of eCO_2R performance (FE_{CO} vs potential) between Ag_{21} and recent catalysts. S20

Table S3. Interaction energies E_{int} of Ag_{21} and Ag_{42} with MCT/CBDT and TPP ligands in eV units S21

Table S4. Bader charge on different Ag atoms in Ag_{21} clusters S21

Table S5. Bader charge on different Ag atoms in Ag_{21} clusters S22

5. References S23

1. Instrumental details and characterization

UV-vis absorption spectra of clusters were recorded using a Perkin Elmer Lambda-1050 UV–Vis-NIR spectrophotometer. The electrospray ionization mass spectra (ESI-MS) of nanoclusters (NCs) were acquired on a Waters Synapt G2Si HDMS instrument. ESI-MS instrumental parameters were maintained with the following values: capillary voltage, 2-3 kV; source temperature, 80-100 °C; flow rate, 15-20 μL/min; cone voltage, 20 V. Ag_{21} and Ag_{42} spectra were recorded in positive ion mode, whereas Ag_{31} was recorded in negative mode. Fourier-transform infrared (FTIR) spectrum was collected from KBr pellets in the range of 3000 - 500 cm^{-1} with a JASCO-4100 FT-IR spectrometer. For the spectral measurement, microcrystalline samples were positioned on top of the diamond crystal. For understanding the morphological features of silver clusters, scanning electron microscopy (SEM) and high-resolution transmission electron microscopy (HR-TEM) have been performed on the AgNCs samples. For imaging of the clusters, SEM, JSM-6500F, JEOL, has been used. Using a field emission gun running at 200kV, the Talos F200X, JEOL, and JSM-2010F were utilized to acquire the cluster images. A cold-field emission gun and a high-angle silicon drift energy dispersive X-ray (EDX) detector for elemental mapping were incorporated with this 80 kV device.

A JEOL-3010, 300 kV device was used to measure transmission electron microscopy (TEM). The images were taken using a Gatan 794 multiscan CCD camera. For XPS (X-ray photoelectron spectroscopy) characterization studies, PHI Quantera XPS and 1486.68 eV Al Kα X-ray source were used. The shift in the binding energy due to the buildup of charges from insulating samples (mainly from organic ligands) is corrected by the carbon 1s correction. C1s, S2p, N1s, O1s, Ag3d, P2p, and B1s signals of the three different clusters were deconvoluted and fitted using the Fityk software and the Gaussian-Lorentzian function. To study and investigate the local oxidation state and coordination number to which each of the Ag atoms is bonded, XAS (X-ray Absorption Spectroscopy) was conducted at the BL01C1 beamline of TLS, NSRRC. Ag K-edge measurements (25,514 eV) were conducted in fluorescence mode. The XAS results were processed using Athena software, with normalization to the incident beam intensity. Beam energy calibration was performed at the first inflection point of the Ag absorption edge using an Ag foil as a reference.

2. Computational Details

The first principle spin-polarized calculations were performed using the Vienna *ab initio* simulation package (VASP).[1,2] The Generalized Gradient approximation with Perdew-Burke-Ernzerhof (GGA-PBE) was employed to describe the exchange-correlations functionals and the Projector Augmented Wave (PAW) was utilized to describe the ion core and valence electron interactions.[3,4] The cutoff energy for the plane-wave basis sets was set to 470 eV and a conjugate-gradient algorithm with an energy convergence criterion of 10^{-4} and Hellman-Feynman force convergence criteria of < 0.02 eVÅ^{-1} was utilized during structural optimizations. Gaussian smearing of 0.2 eV and the DFT-D3 method were used to correctly define the van der Waals interactions.[5] All the spin-polarized calculations were performed for all the oxygen-adsorbed intermediates and molecular species. The Gibbs free energies of elementary steps during the CO_2RR were calculated using the computational hydrogen electrode (CHE) model proposed by Nørskov and co-workers by using the following equation:[6]

$$\Delta G = \Delta E + \Delta ZPE + T\Delta S - eU \quad \textbf{(S1)}$$

where ΔE is the total energy change in the reaction, ΔZPE is the change in the zero-point energy, T is 300 K temperature, ΔS is the entropy change, U is the electrode potential referenced to the standard hydrogen electrode, and *e* is the transferred electronic charge. The ZPE and entropies were calculated from harmonic oscillator approximation using the following formula:

$$ZPE = \sum_i \frac{1}{2} h\nu_i \quad \textbf{(S2)}$$

$$S_v = R \sum \frac{\hbar\nu_i}{k_B T\left(\exp\left(\frac{\hbar\nu_i}{kT}-1\right)\right)} - \ln\left(1 - \exp\left(\frac{\hbar\nu_i}{kT}\right)\right) \quad \textbf{(S3)}$$

where h is the Planck constant, S_v is the vibrational entropy, R is the gas constant, k_B is the Boltzmann constant, ν_i is the frequency of the i_{th} vibrational mode and $\hbar = h/2\pi$. The single molecular unit cell Ag_{21} and Ag_{42} were optimized in 30 × 35 × 35 Å^3, to minimize the interactions between periodic images. The Γ-centered (1×1×1) k-point grids were considered for the sampling of the Brillouin zone considering the large size of the box. A higher (3 × 3 × 3) k-mesh was used to calculate the density of states (DOS). Bader atomic charges were determined using the Henkelman code with the near-grid algorithm refine edge method.[7,8] All of the isosurface values for the charge density difference analysis were set to be 0.002 eV Å^{-3}, where pink and blue colors gradients represent charge depletion and accumulation regions, respectively.

3. Figures

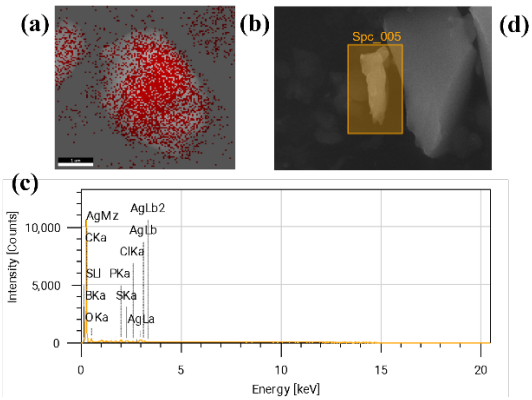

(d)

Element	Line	Mass%	Atom%
B	K	6.27±0.04	7.26±0.05
C	K	83.24±0.19	86.79±0.20
O	K	6.63±0.15	5.19±0.12
P	K	0.52±0.02	0.21±0.01
S	K	0.44±0.02	0.17±0.01
Ag	L	2.90±0.08	0.37±0.01
Total		100.00	100.00
Spc_005		Fitting ratio 0.0114	

Figure S1. (a, b) SEM-EDS images of Ag_{21} NC (c) EDS spectra of Ag_{21} NC, d) All the elements present in Ag_{21} and its corresponding mass percentage and atomic percentage

Figure S2. Photographic images of UV-visible samples of a) Ag_{21}, b) Ag_{31}, c) Ag_{42}

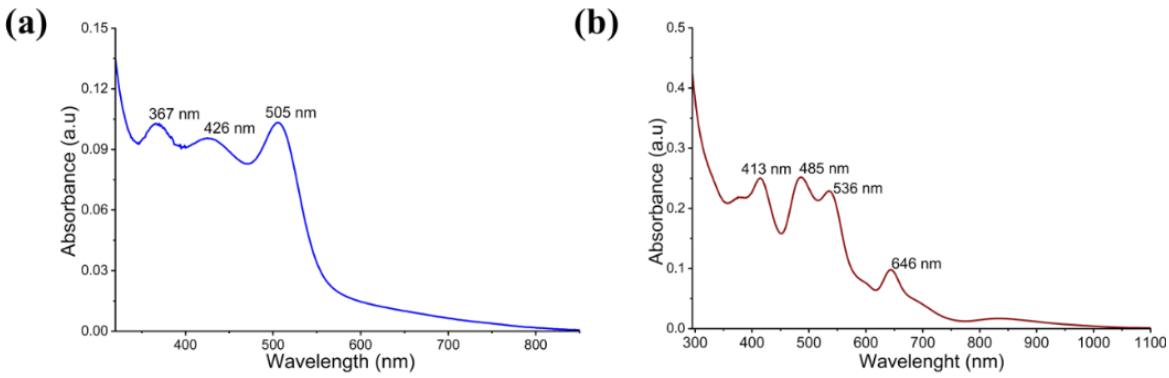

Figure S3. UV-vis absorption spectra of (a) Ag_{22}, (b) Ag_{44} before loading the GDE

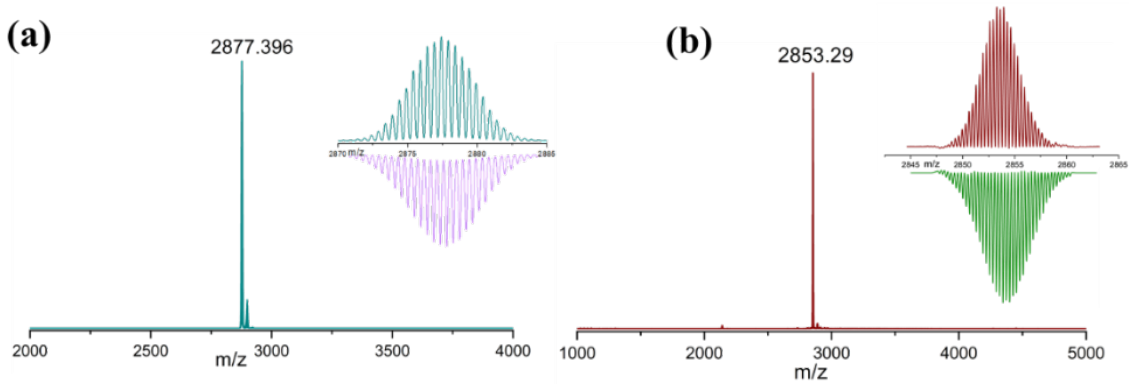

Figure S4. High-resolution mass spectrometric data of the catalyst materials before GDE loading, with inset showing the comparison of respective experimental and simulated spectra, (a) Ag_{22} (b) Ag_{44}

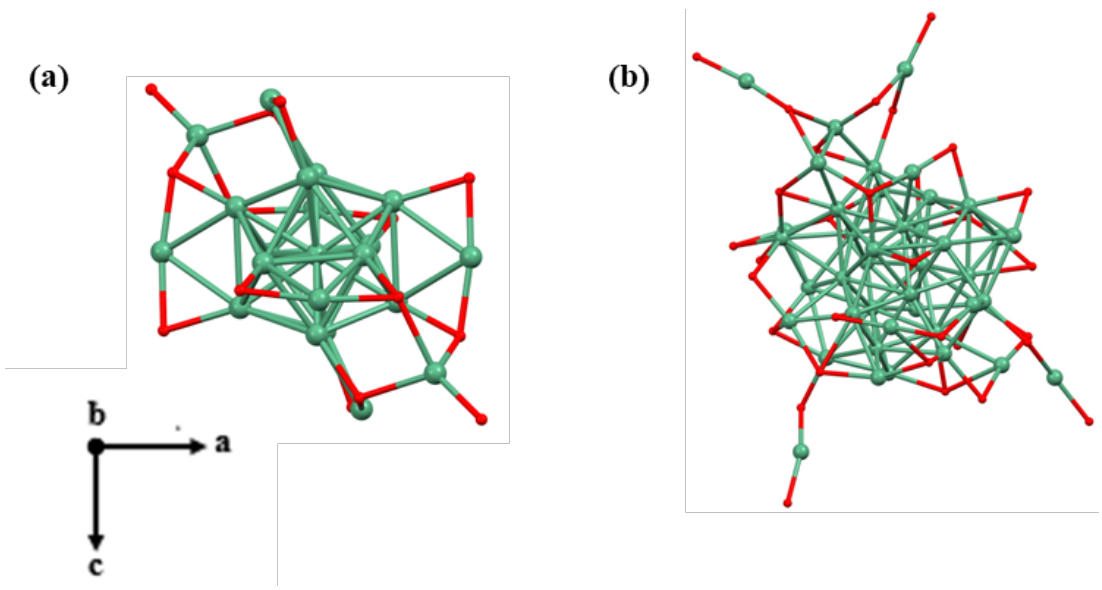

Figure S5. The metal core structure of (a) Ag_{21} NC (from SCXRD) (b) Ag_{42} NC (DFT optimized structure). Both structures are aligned in the direction of the b-axis. Colour code - Dark green: silver, Red: sulfur.

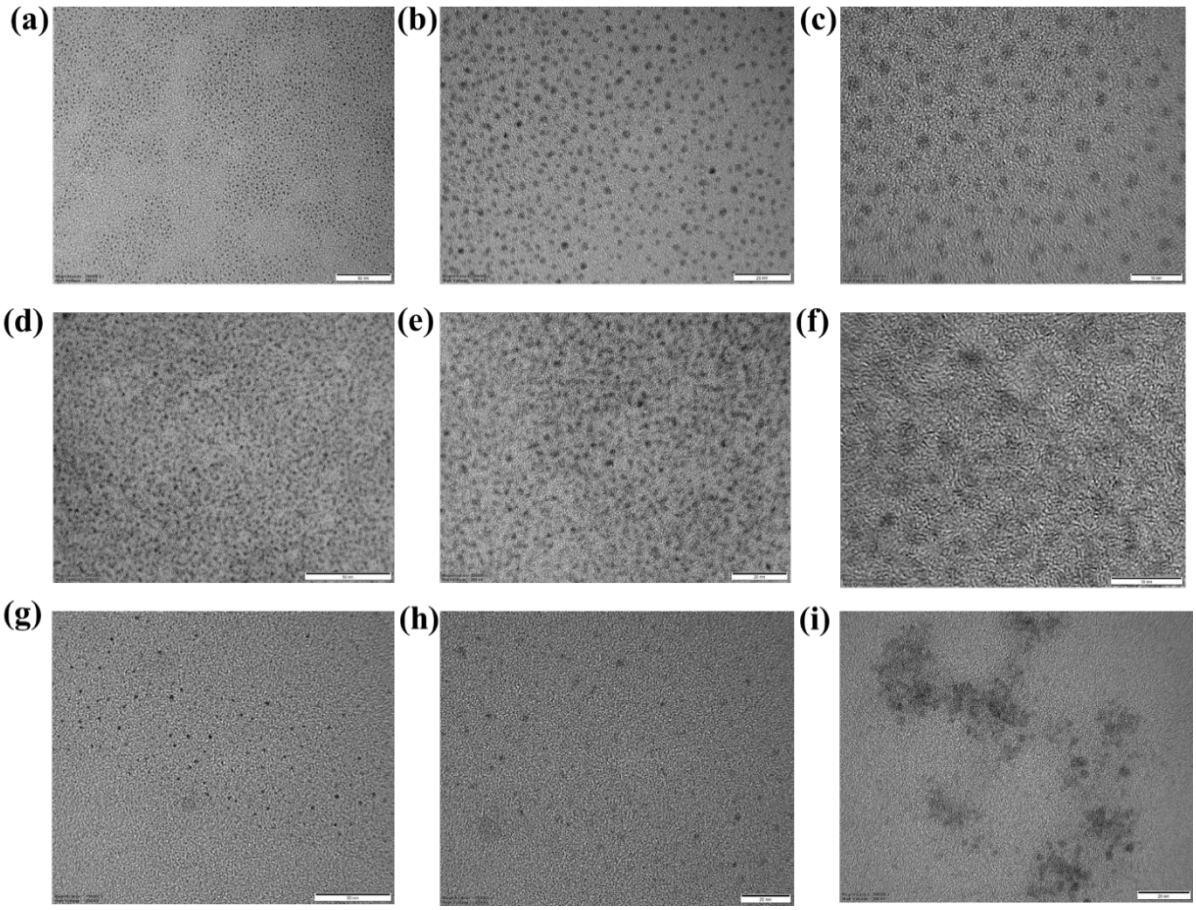

Figure S6. TEM images of Ag NCs (a-c) Ag_{21}, (d-f) Ag_{31}, (g-i) Ag_{42}

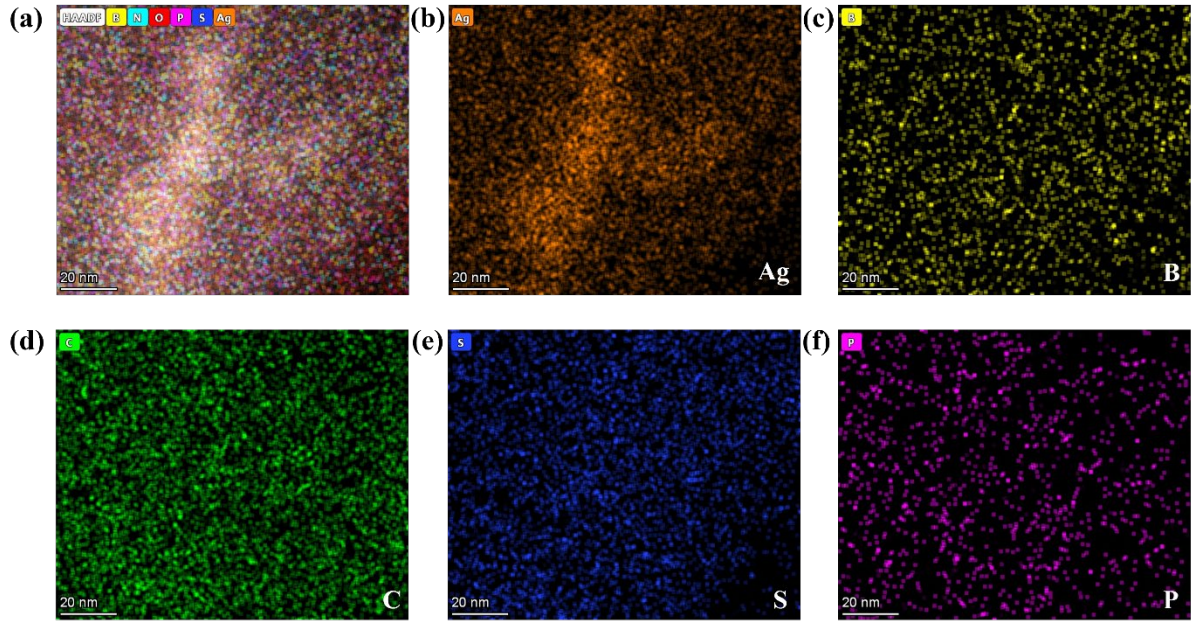

Figure S7. HAADF STEM elemental mapping of Ag_{21} NC

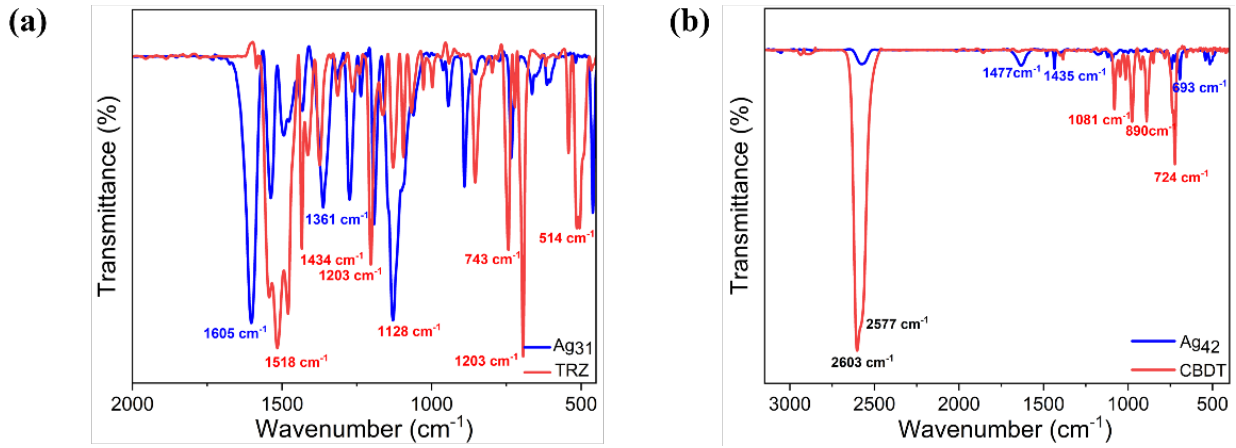

Figure S8. FTIR Spectra of (a) Ag_{31} and TRZ, (b) Ag_{42} and CBDT

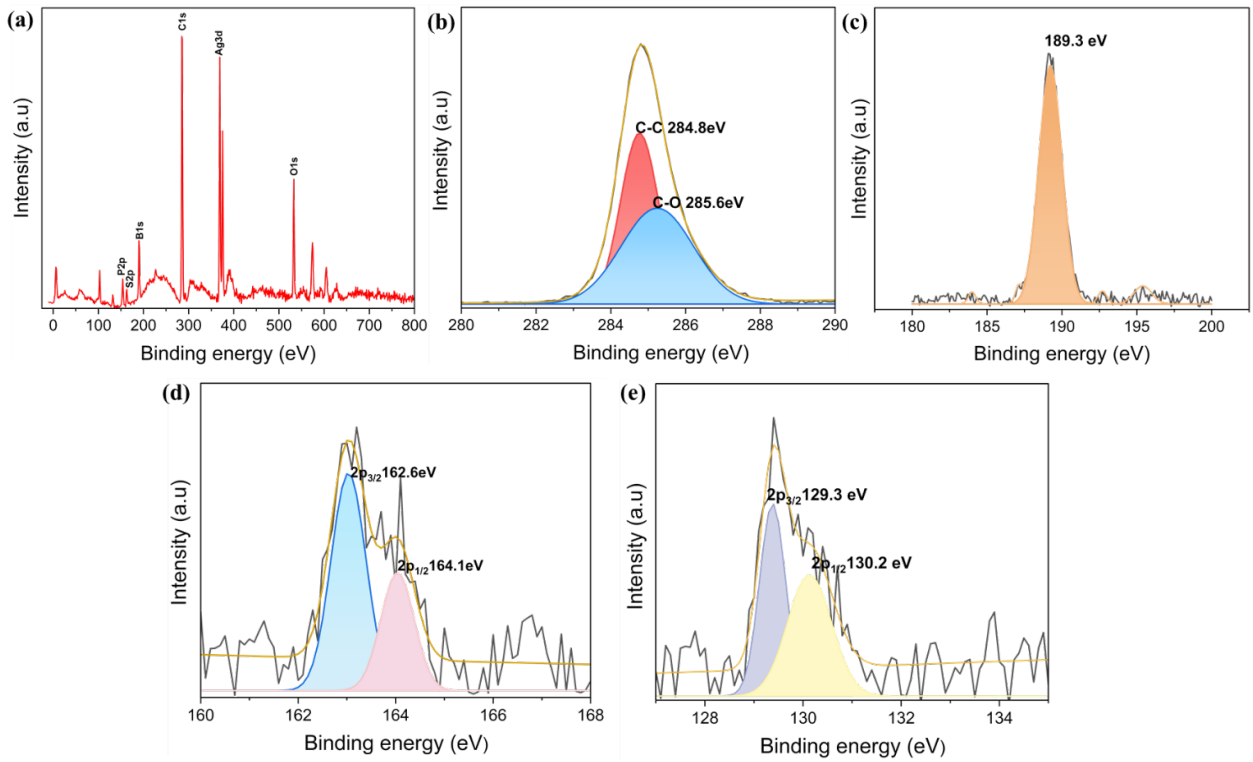

Figure S9. HR-Elemental XPS scans and peak fitting of Ag_{21} NC catalysts. (a) Full scan survey XPS (b) C1s, (c) B1s (d) S2p e) P2p

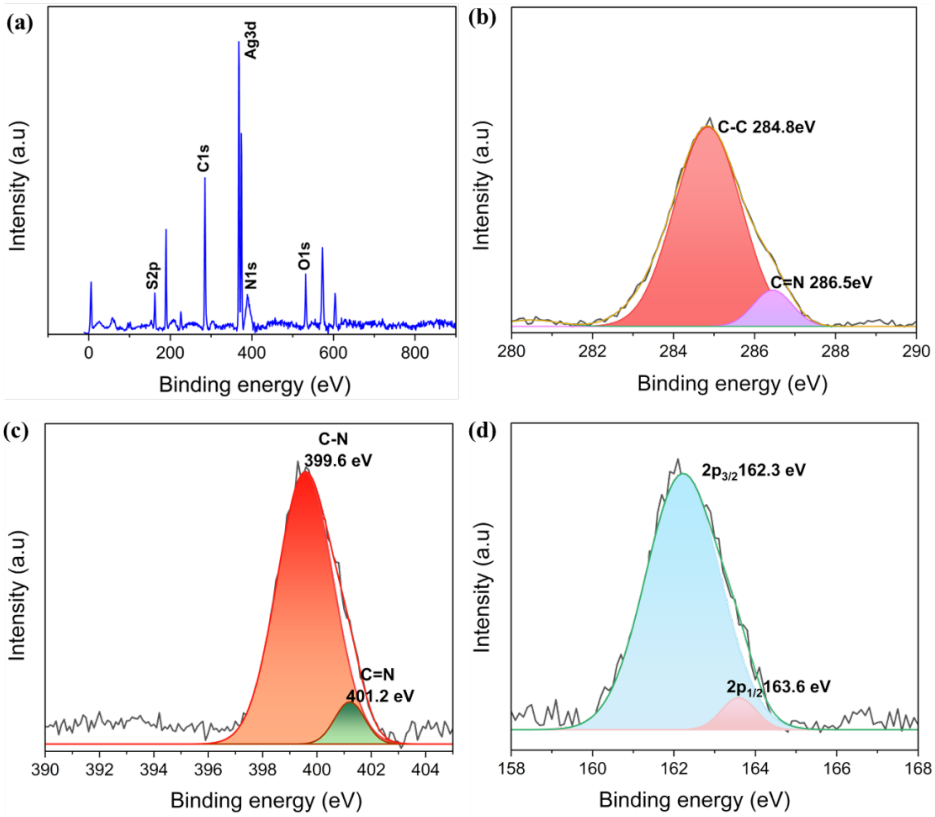

Figure S10. HR-Elemental XPS scans and peak fitting of Ag_{31} NC catalysts. (a) Full scan survey XPS b) C1s (c) N 1s, (d) S 2p

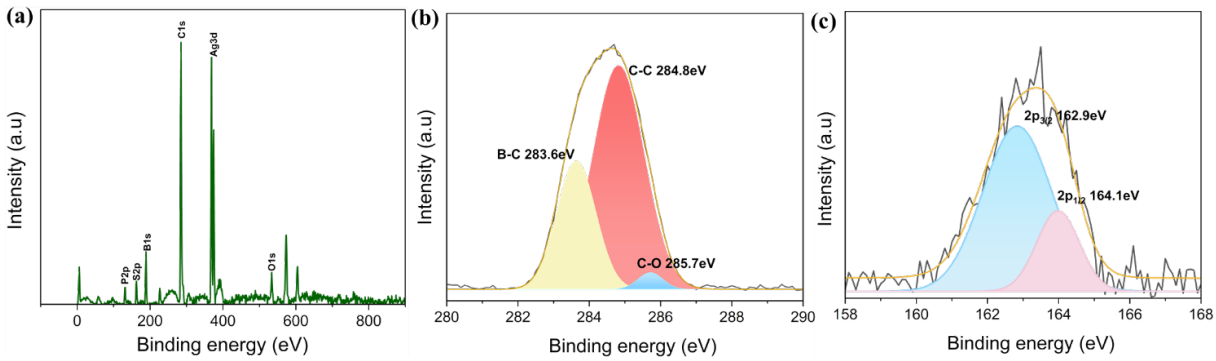

Figure S11. HR-Elemental XPS scans and peak fitting of Ag_{42} NC catalysts. (a) Full scan survey XPS (b) C 1s (c) S 2p

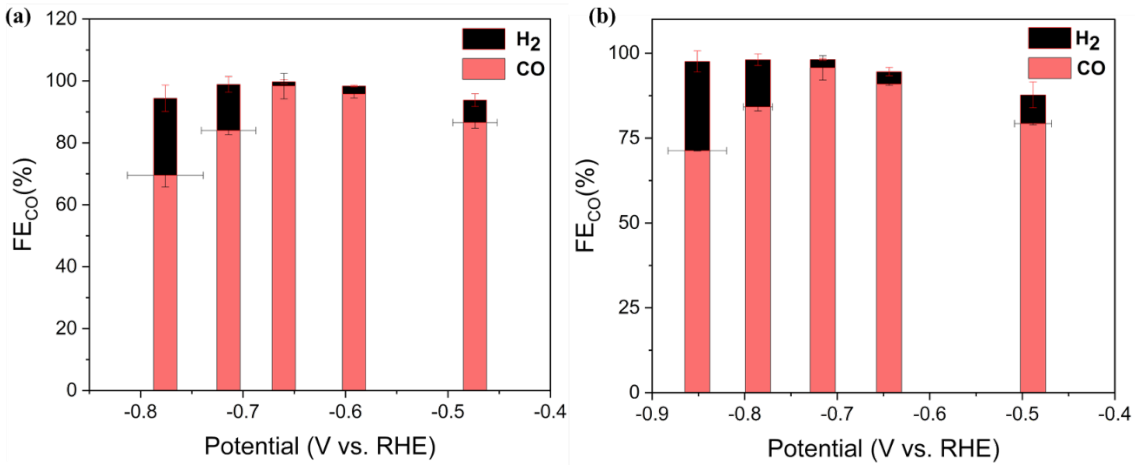

Figure S12. eCO_2R performance of Ag NCs in 1 M KOH in an alkaline flow cell. FE (%) of CO vs potential for (a) Ag_{31} NC (b) Ag_{42} NC

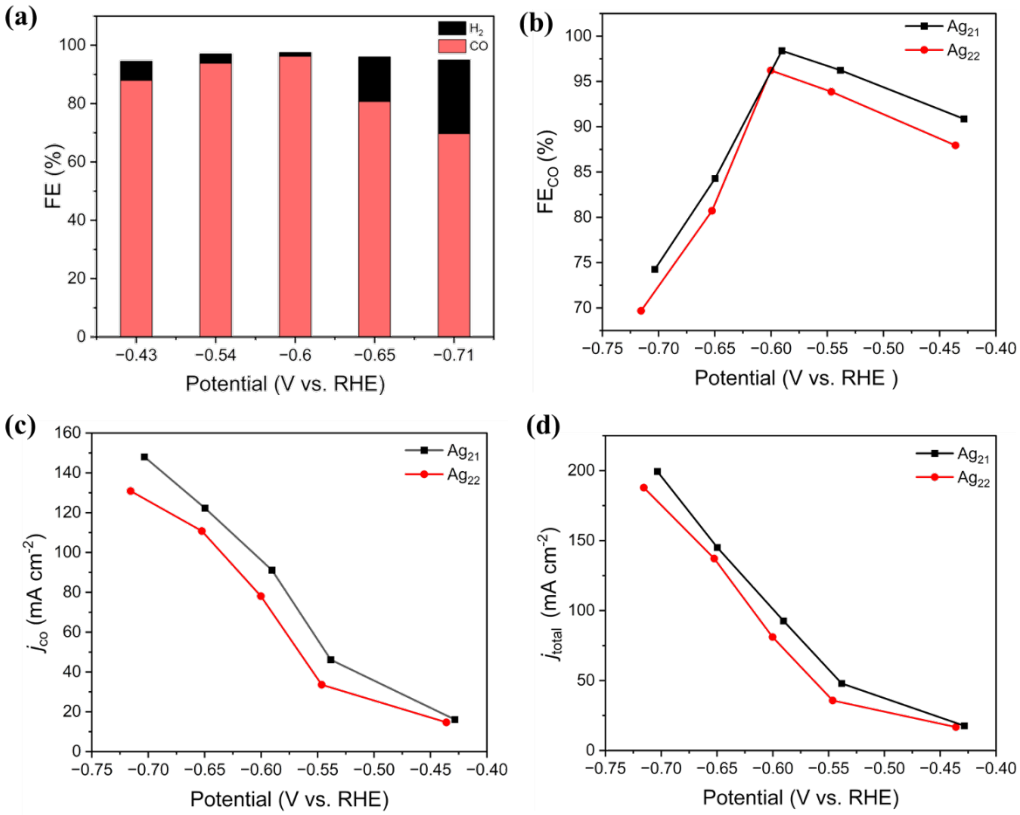

Figure S13. eCO_2R performance of Ag_{22} in 1 M KOH in an alkaline flow cell. (a) FE (%) of products with varying potential, (b) FE (%) of CO with varying potential in comparison with Ag_{21} (c) partial current density for CO across the potential range in comparison with Ag_{21} (d) (d) total current density across the potential range in comparison with Ag_{21}

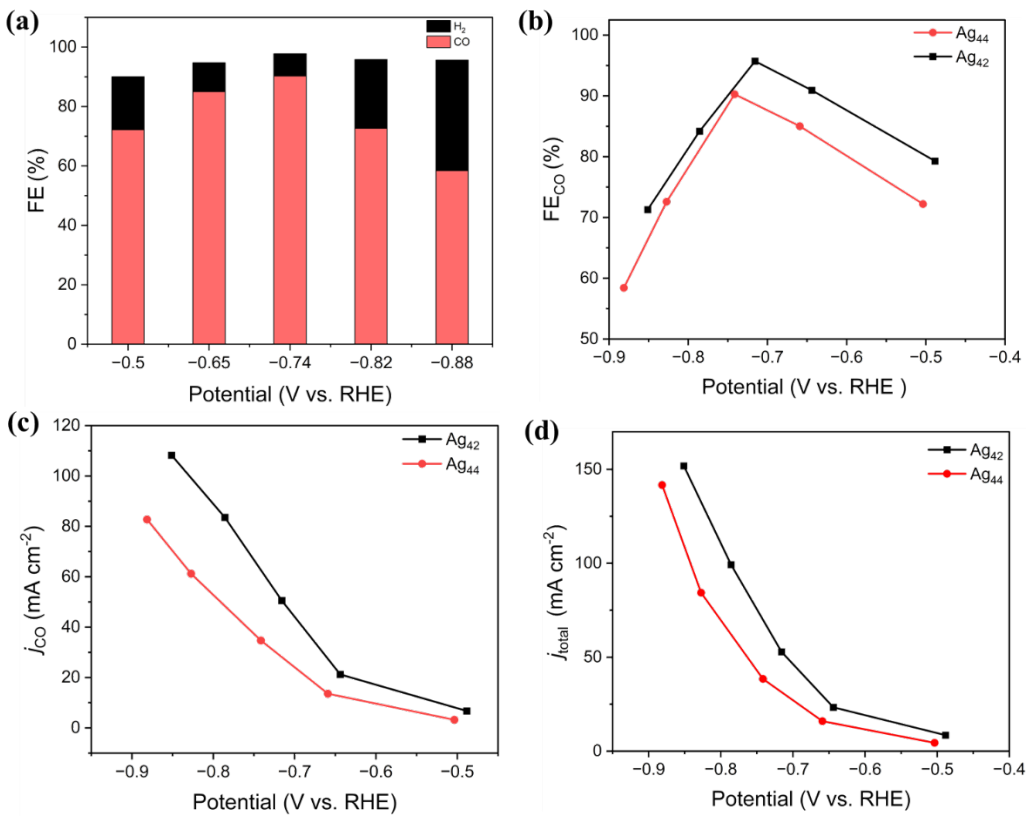

Figure S14. eCO_2R performance of Ag_{44} in 1 M KOH in an alkaline flow cell. (a) FE (%) of products with varying potential, (b) FE (%) of CO with varying potential in comparison with Ag_{42} (c) partial current density for CO across the potential range in comparison with Ag_{42} d) (d) total current density across the potential range in comparison with Ag_{42}

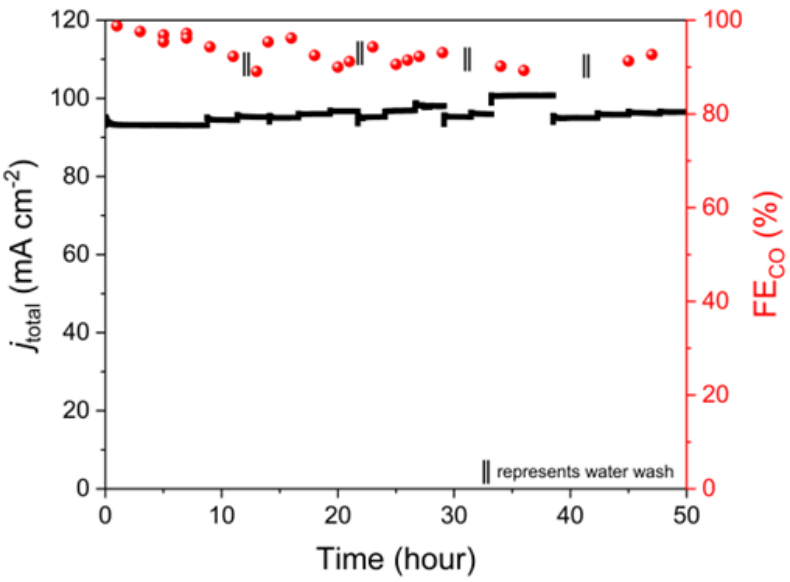

Figure S15. (e) Electrocatalytic Stability plot of Ag_{21} measured at a constant voltage of 0.59V vs RHE for 50 hours

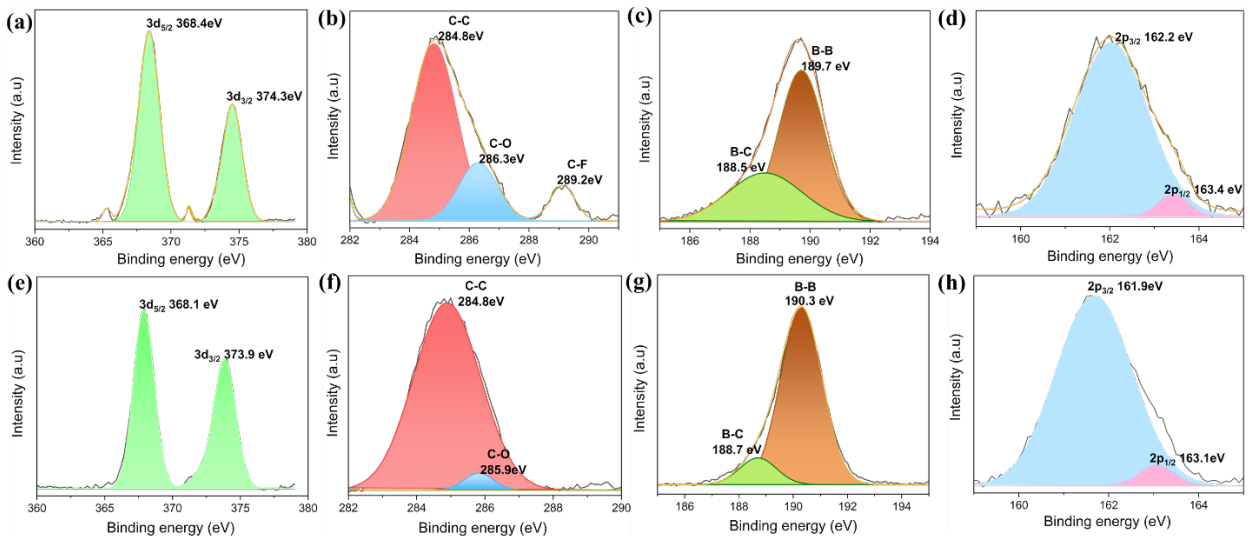

Figure S16. Pre- and post-electrochemical XPS peak fitting of Ag_{21} NC catalyst-coated electrode. (a, e) Ag3d, (b, f) C1s, (c, g) B1s, and (d, h) S2p respectively

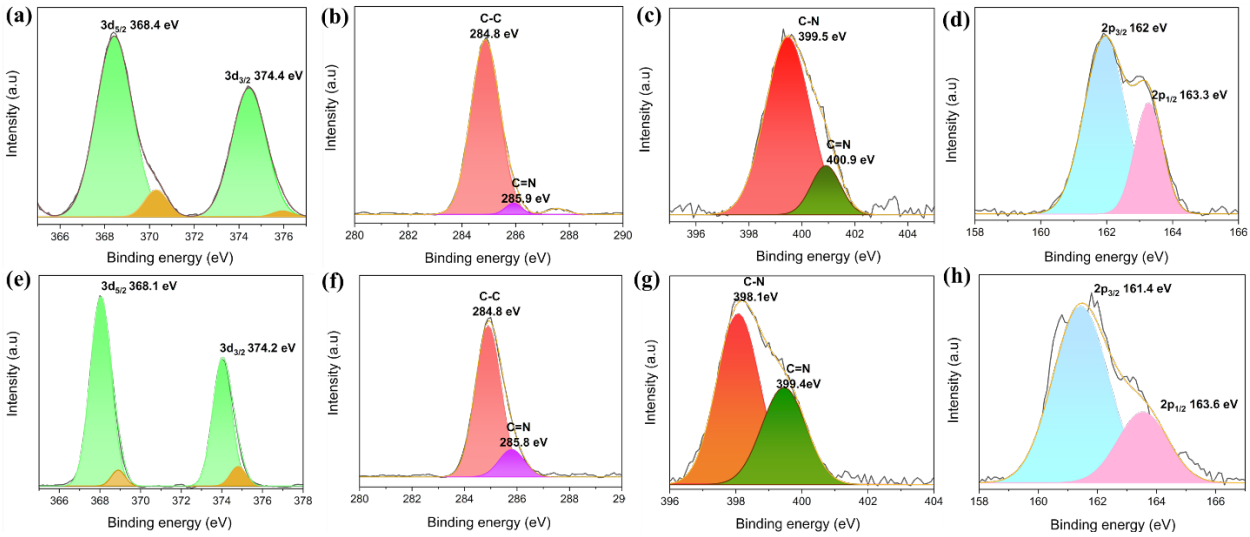

Figure S17. Pre- and post-electrochemical XPS peak fitting of Ag_{31} NC catalyst-coated electrode. (a, e) Ag3d, (b, f) C1s, (c, g) N 1s, and (d, h) S 2p.

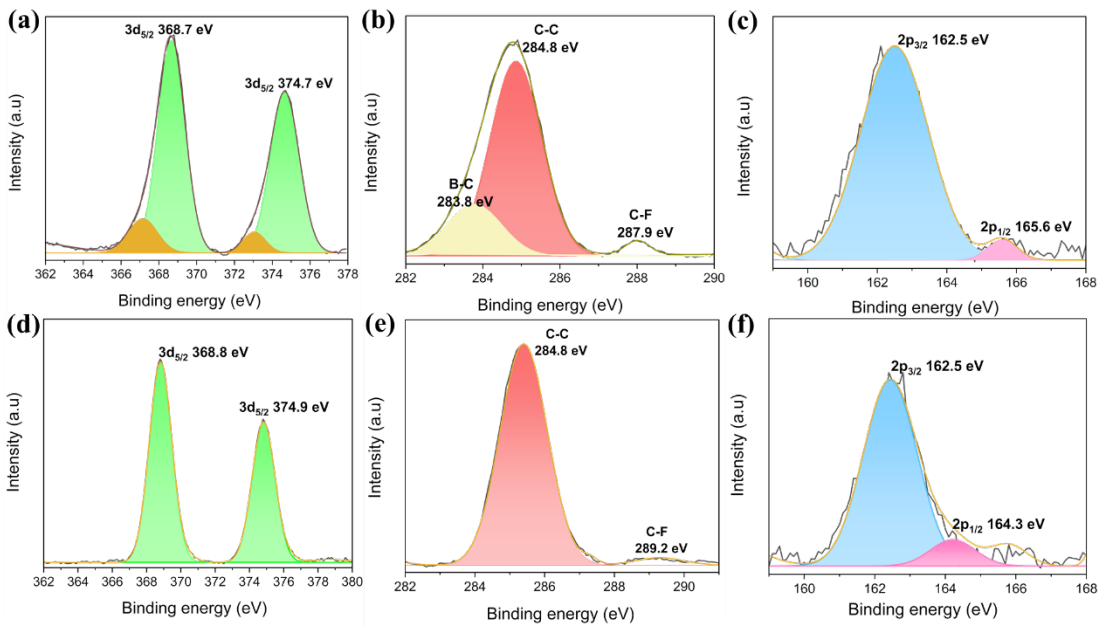

Figure S18. Pre- and post-electrochemical XPS peak fitting of Ag_{42} NC catalyst-coated electrode. (a, d) Ag3d, (b, e) C1s, (c, f) S 2p.

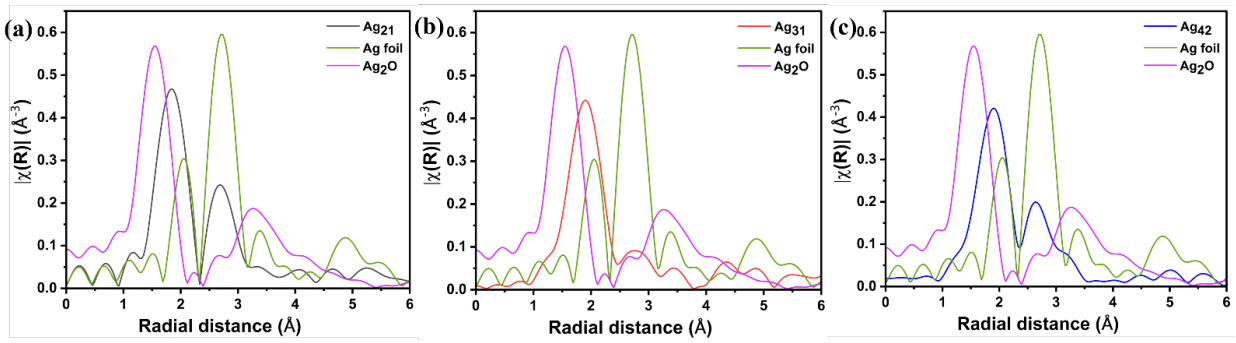

Figure S19. EXAFS spectra of Ag K edge for the AgNCs post eCO_2R

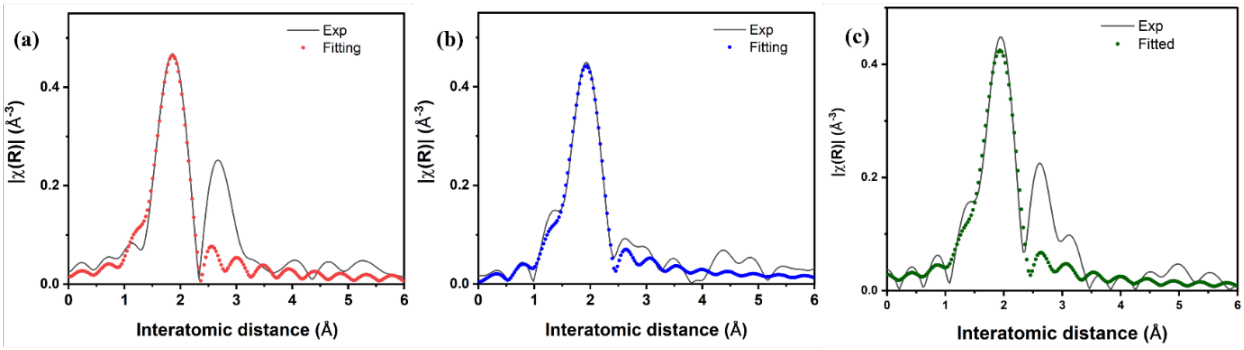

Figure S20. EXAFS fitting result of (a) Ag_{21} NC (b) Ag_{31} NC (c) Ag_{42} NC at R space post eCO_2R

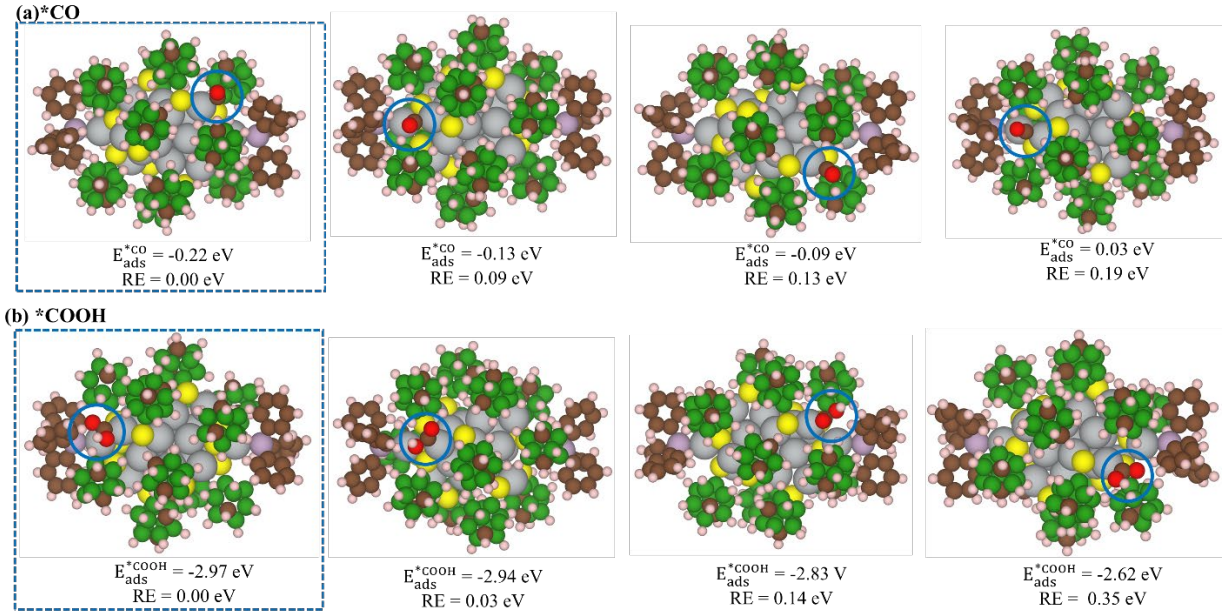

Figure S21. Heterogeneous Active Sites Investigated for **(a)** *CO, and **(b)** *COOH adsorption on the Ag_{21} cluster, with E_{Ads}^{*COOH} representing adsorption energy in eV. The most stable configurations are highlighted with blue boxes.

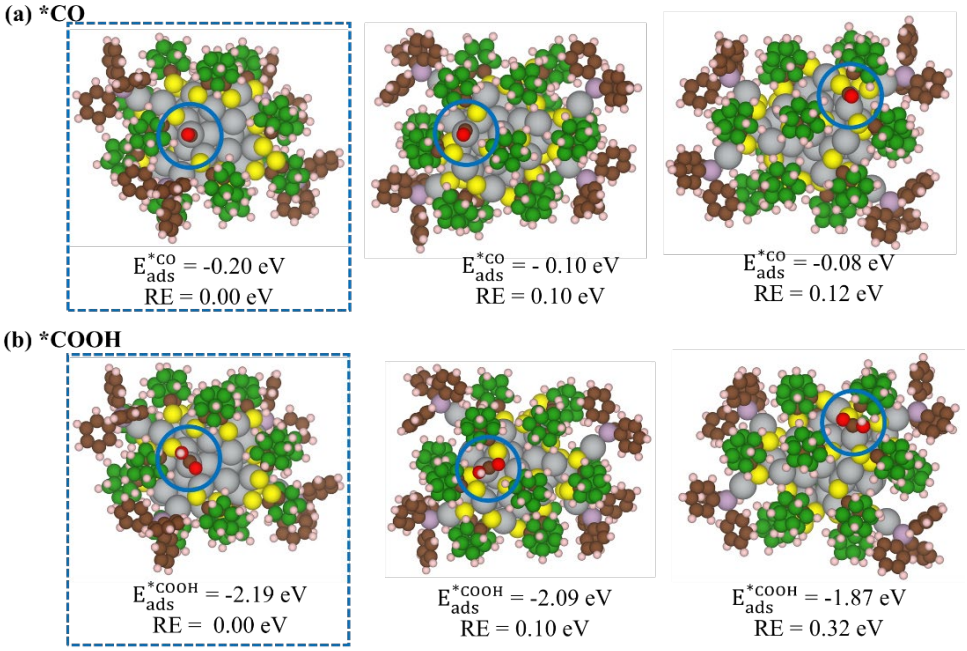

Figure S22. Heterogeneous Active Sites Investigated for **(a)** *CO, and **(b)** *COOH adsorption on the Ag_{42} cluster, with E_{Ads}^{*COOH} representing adsorption energy in eV. The most stable configurations are highlighted with blue boxes.

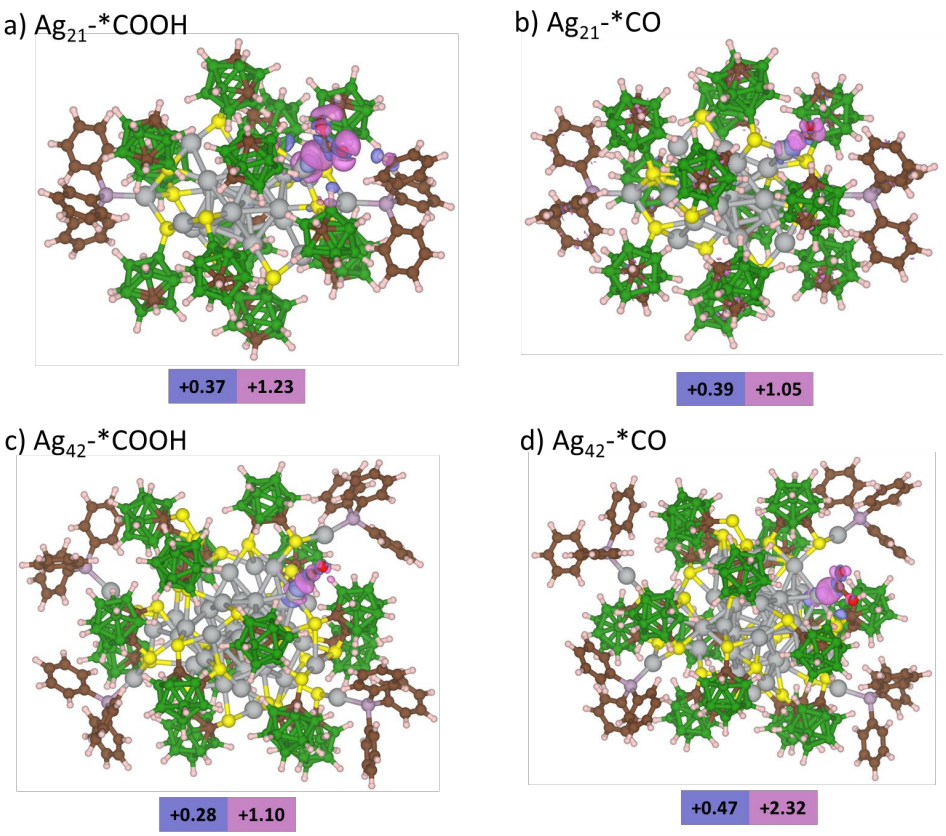

Figure S23: Charge density difference (CDD) plots at an isosurface of 0.002 eV/Å^3, where pink and green regions indicate charge accumulation and depletion, respectively. Numeric values represent charge transfer (in |e| units) derived from Bader charge analysis on Ag and C atom.

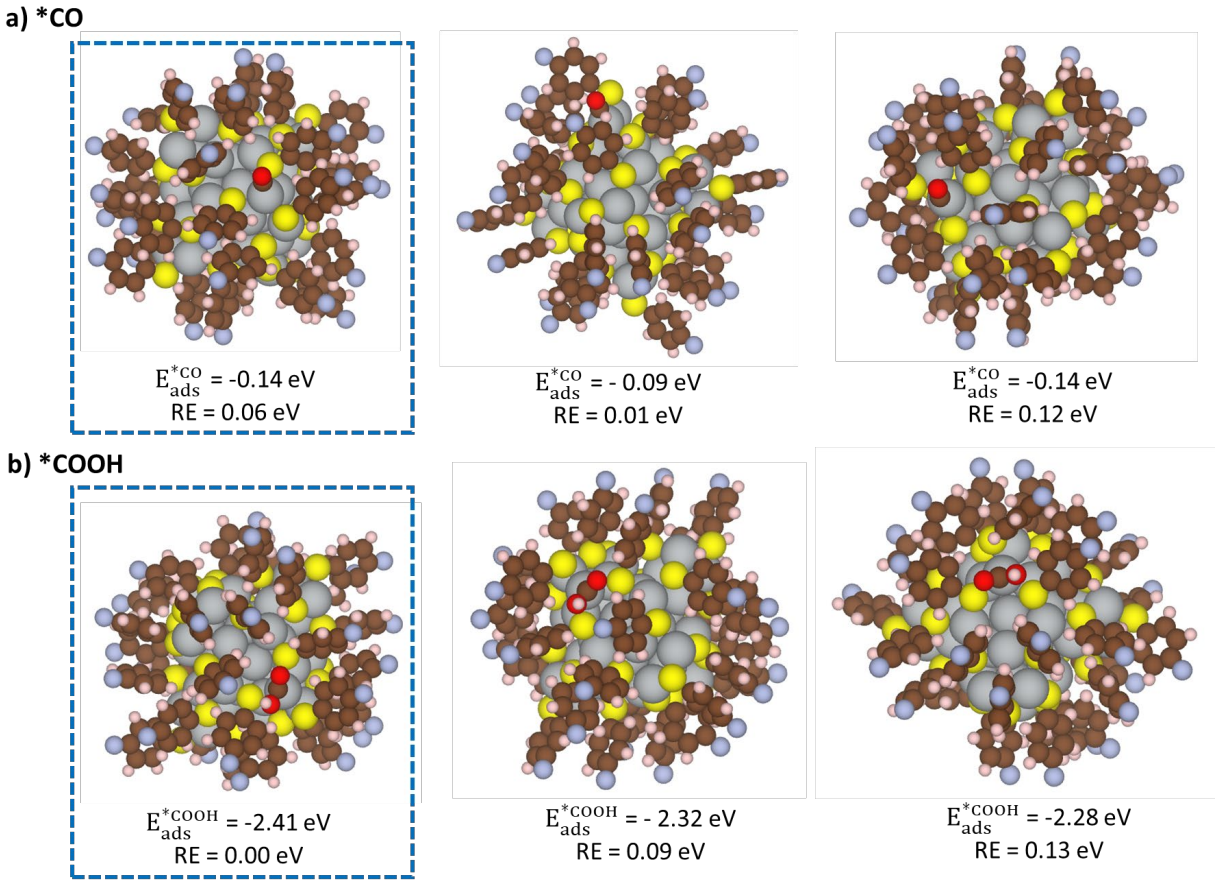

Figure S24. Heterogeneous Active Sites Investigated for **(a)** *CO, and **(b)** *COOH adsorption on the Ag_{44} cluster, with E_{Ads}^{*COOH} representing adsorption energy in eV. The most stable configurations are highlighted with blue boxes. The relative energies (RE) are referenced against the most stable geometries, marked as RE = 0.00 eV.

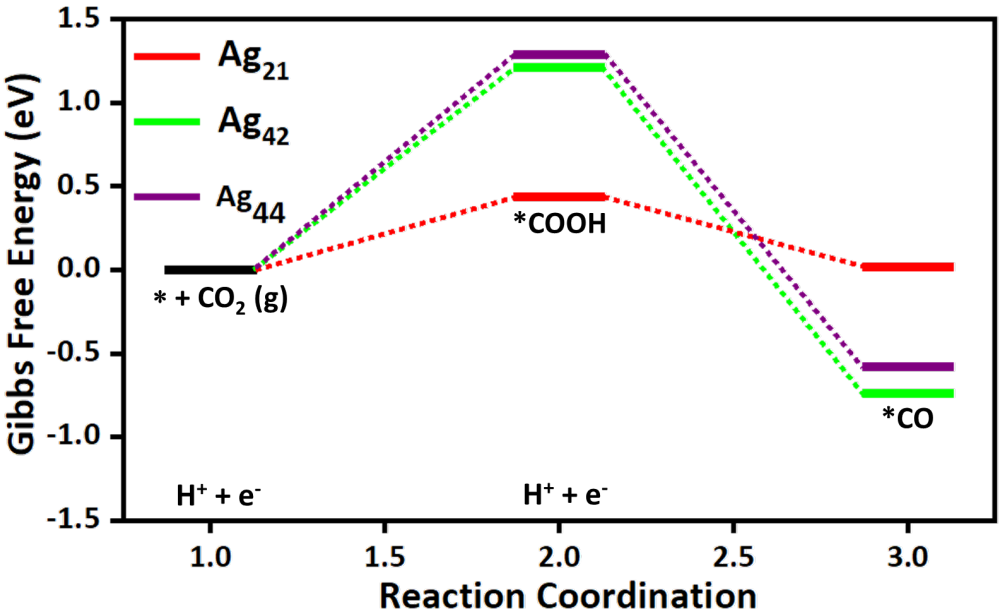

Figure S25. Gibbs free energy diagram of Ag_{21}, Ag_{42}, and Ag_{44} clusters, with the black solid horizontal line denoting the neutral surface reference.

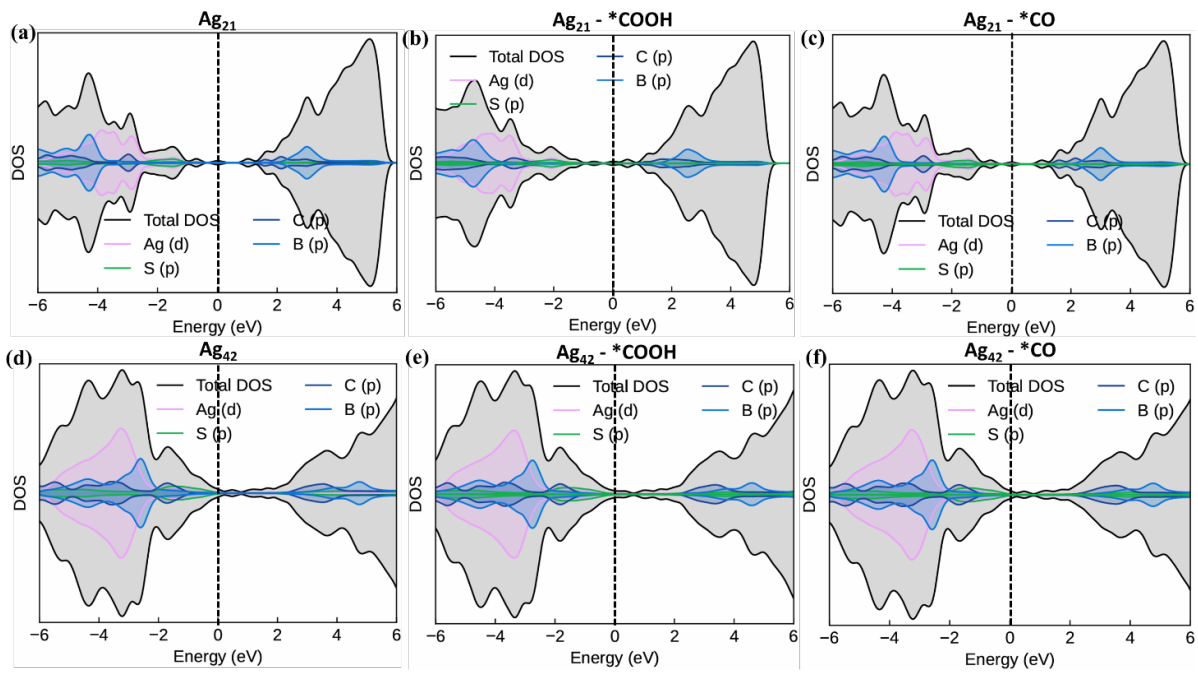

Figure S26. Total and partial DOS analysis for pristine, *COOH, and *CO-adsorbed Ag_{21} and Ag_{42} clusters, with the Fermi-level set at 0.00 eV.

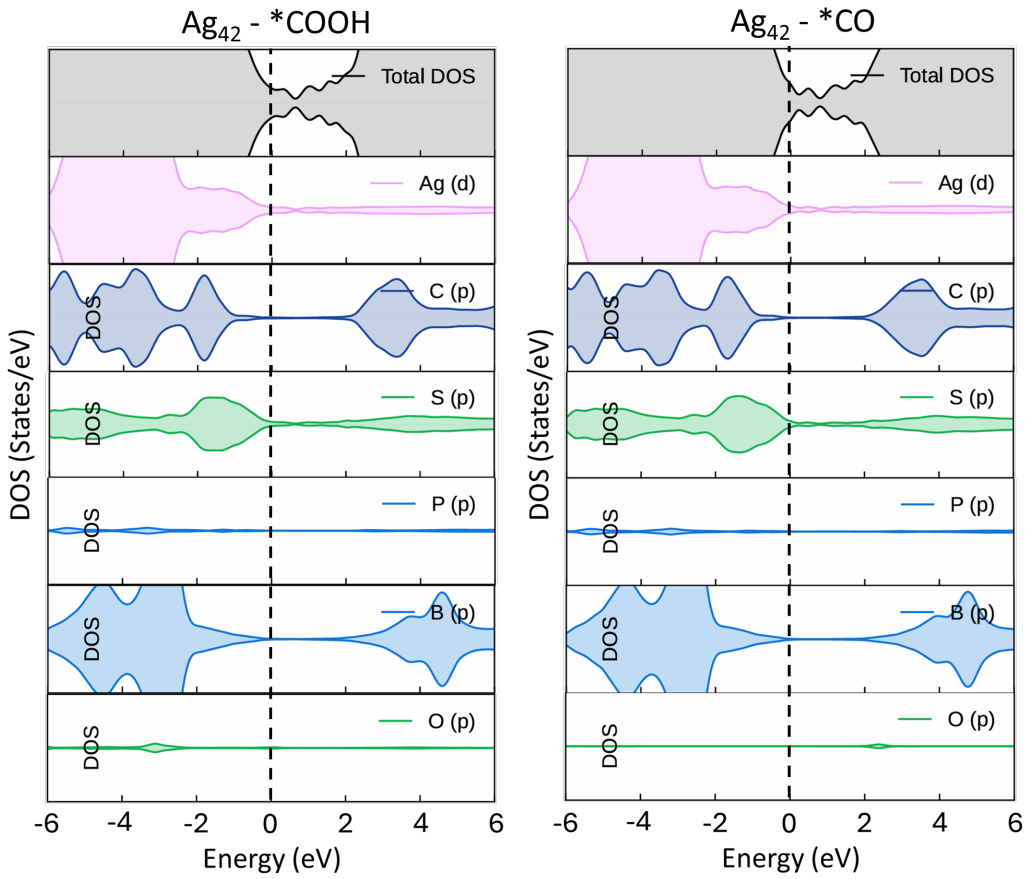

Figure S27. Subplots for total and partial density of states (DOS) for Ag(5d), C(p), S(p), P(p), B(p), and O(p), respectively, with the Fermi-level set at 0.00 eV for **(a)** *COOH, and **(b)** *CO-adsorbed on Ag_{42}.

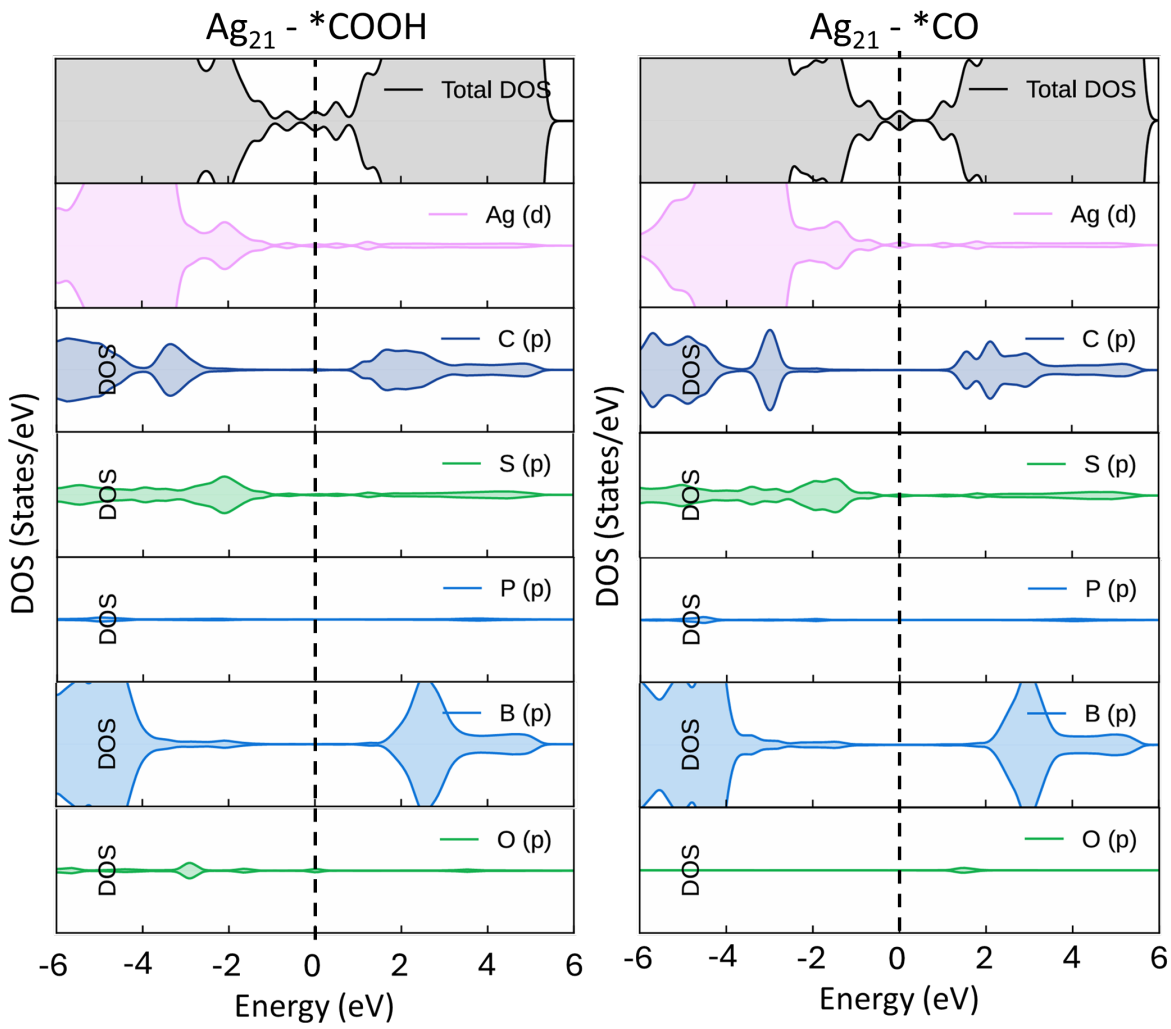

Figure S28. Subplots for total and partial density of states (DOS) for Ag(5d), C(p), S(p), P(p), B(p), and O(p), respectively, with the Fermi-level set at 0.00 eV for **(a)** *COOH, and **(b)** *CO-adsorbed on Ag_{21}.

4. Tables

Table S1. EXAFS fitting parameters of Ag NC catalysts.

	path	N	R	dE	DW	R factor
Ag_{21}	Ag-S	0.9 ± 0.1	2.40 ± 0.02	-0.7 ± 0.5	0.007	0.0048
Ag_{31}-before	Ag-S	1.1 ± 0.1	2.47 ± 0.02	-1.0 ± 0.4	0.009	0.0025
Ag_{31}-after	Ag-S	1.5 ± 0.3	2.46 ± 0.04	-3.2 ± 0.6	0.008	0.0081
Ag_{41}	Ag-S	1.0 ± 0.3	2.46 ± 0.07	3.4 ± 0.9	0.009	0.0106

Table S2: Comparison between Ag_{21} and the most advanced Ag-based catalysts (mostly reported clusters) for eCO_2R in terms of maximum partial current density (j_{CO}) and maximum Faradaic efficiency for CO (FE_{CO})

	Catalyst	Max FE_{CO} (%)	E_0 for max FE_{CO} (V vs. RHE)	Max j_{CO} (mA cm^{-2})	Cell setup	Electrolyte	Reference
	$[Ag_{21}(MCT)_{12}(TPP)_2]^+$	99.6	-0.59	148	Flow cell	1 M KOH	This work
X1	$Ag_{19}Cu_2(C \equiv CAr^F)_{12}(PPh_3)_6Cl_6$	95.26	-1.3	257.2	NA	1 M KOH	Nanoscale.2024;16(36):16952-7.[9]
X2	Ag-CP	>96	-1.0	385	Flow cell	0.1 M $KHCO_3$	ACS Energy Lett. 2019, 4, 8, 2024–2031[10]
X3	NiAD/AgNPs@CN	>90	-0.88	79.7	Flow cell	0.1 M $KHCO_3$	Applied Catalysis B: Environment and Energy. 2024 Jul 15;349:123886[11]
X4	Ag-Zn-ZIF-8 (10% Ag, 90% Zn)	80	-0.9	9	Flow cell	0.1 M $KHCO_3$	Catalysts. 2023 May 10;13(5):867.[12]
X5	$ClAg_{14}$ $(C \equiv CBu)_{12}$	95	-0.5	285	Flow cell	1 M KOH	Advanced Science. 2024 Mar;11(10):2306089.[13]
X6	$Ag_{25}(SPhMe_2)_{18}$	80	~-0.65	94	Flow cell	1 M KOH	Advanced Science. 2024 Mar;11(10):2306089.[13]
X7	$Ag_{12}Cu_7(4^tBuPhC{\equiv}C)_{14}(Dpppe)_3Cl_3(SbF_6)_2$	71.2	-1.17 V	117.9	Flow cell	1 M KOH	ACS Cent. Sci. 2025, 11, 8, 1428–1437[14]
X8	Ag@C NPs	90	-0.55	300	Flow cell	1M KOH	Cell Reports Physical Science. 2022 Jul 20;3(7)[15]
X9	Ag/MWNC	>95	-0.77	338	Flow cell	1 M KOH	Journal of Materials Chemistry A. 2016;4(22):8573-8[16]
X10	$Ag_{15}(C{\equiv}C{-}CH_3)^+$	~96	2V (Ag/AgCl)	92	Flow cell	1 M NaCl	J. Am. Chem. Soc. 2025, 147, 3, 2699–2713[17]
X11	$AuAg_{24}(IPBT)_{18}$	90	-3.6 (Cell Voltage)	200	MEA cell	0.5 M $KHCO_3$	J Am Chem Soc. 2025 Apr 16;147(15):12546-12554.[18]
X12	$[Ag_{15}Cu_6(C{\equiv}CR)_{18}(DPPE)_2]^-$	90.6	-3.75 (Cell Voltage)	40	MEA cell	0.1 M $KHCO_3$	J. Am. Chem. Soc. 2023, 145, 6, 3401–3407[19]
X13	5 nm Ag/C	79.20	~-0.75	8	H- cell	0.5 M $KHCO_3$	J. Am. Chem. Soc. 2015, 137, 43, 13844–13850[20]
X14	$Ag_{15}(C{=}C\text{-}tBu)_{12}^+$	95	-0.6	~21	H-cell	0.5 M $KHCO_3$	Angewandte Chemie International Edition. 2021 Dec 6;60(50):26136-41.[21]
X15	$[Ag_{15}Cu_6(C{\equiv}CR)_{18}(DPPE)_2]^-$	91	-0.81	~18	H-cell	0.1 M $KHCO_3$	J. Am. Chem. Soc. 2023, 145, 6, 3401–3407[19]
X16	$(AuAg)_{44}(C_{10}H_9)_{28}$	98	-0.8	~18	H-cell	0.5 M $KHCO_3$	Chem. Eur. J. 2022, 28, e202201262[22]
X17	$AuAg_{24}(IPBT)_{18}$	70	-0.6	-24.1	H-cell	0.5 M $KHCO_3$	J. Am. Chem. Soc. 2025, 147, 15, 12546–12554[18]
X18	$PtAg_{24}(IPBT)_{18}$	30	لَي	-5.8	H-cell	0.5 M $KHCO_3$	J. Am. Chem. Soc. 2025, 147, 15, 12546–12554[18]
X19	Ag_1/MnO_2	95.7	- c0.85	3.4	H-cell	0.5 M $KHCO_3$	Angew. Chem. Int. Ed. 2021, 60, 6170 – 6176[23]
X20	2D Ag Superstructures	92.5	-0.8	6.82	H-cell	0.1 M $KHCO_3$	ACS Nano 2021, 15, 4, 7682–7693[24]
X21	Nanoporous Ag	92	-0.7	36	H-cell	0.5 M $KHCO_3$	Nat. Commun. 5, 1-6 (2014)[25]
X22	Ag foil	70.5	-0.8	7	H-cell	0.5 M $KHCO_3$	J. Am. Chem. Soc. 137, 13844-13850 (2015)[20]

Table S3. Interaction energies (E_{Int}) of Ag_{21} and Ag_{42} with MCT/CBDT and TPP ligands in eV units. The equation used to calculate the E_{Int} follows:

$$E_{Int} = \frac{E_{Complex} - [\, n_1 * E_{L_1} + n_2 * E_{L_2} \,]}{N}$$

where $E_{Complex}$, E_{L_1}, E_{L_2} represent the total electronic energies of Ag complex, MCT/CBDT, and TPP, respectively. And n_1, n_2 and N represents the number of MCT/CBDT, TPP, and the total number of ligands in the Ag complexes.

Cluster	$E_{Complex}$(eV)	E_{L_1}(eV)	E_{L_2}(eV)	n_1	n_2	N	E_{Int} (eV)
Ag_{21}	-2088.40	-124.72	-222.31	12	2	14	-10.54
Ag_{42}	-2971.57	-117.82	-222.36	15	4	19	-16.57

Table S4. Bader charge on different Ag atoms in Ag_{21} clusters, with its core geometry represented below.

Atom	Charge	Atom	Charge	Atom	Charge
Ag1	0.31	**Ag8**	0.13	**Ag15**	0.10
Ag2	0.31	**Ag9**	0.13	**Ag16**	0.10
Ag3	0.32	**Ag10**	0.13	**Ag17**	0.10
Ag4	0.32	**Ag11**	0.13	**Ag18**	0.10
Ag5	0.32	**Ag12**	0.13	**Ag19**	0.10
Ag6	0.32	**Ag13**	0.01	**Ag20**	0.32
Ag7	0.13	**Ag14**	0.10	**Ag21**	0.32

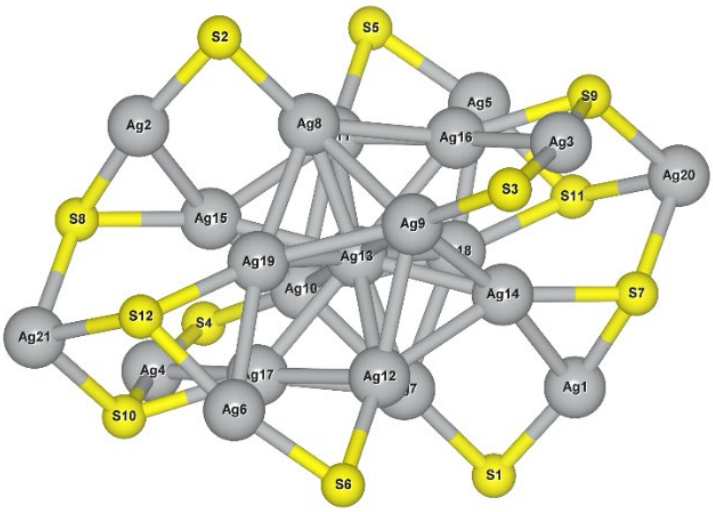

Table S5. Bader charge on different Ag atoms in Ag_{42} clusters, with its core geometry represented below.

Atom	Charge	Atom	Charge	Atom	Charge
Ag1	0.28	**Ag15**	0.30	**Ag29**	0.36
Ag2	0.27	**Ag16**	0.35	**Ag30**	0.31
Ag3	0.19	**Ag17**	0.18	**Ag31**	0.06
Ag4	0.32	**Ag18**	0.18	**Ag32**	0.35
Ag5	0.33	**Ag19**	0.03	**Ag33**	0.00
Ag6	0.18	**Ag20**	0.32	**Ag34**	0.34
Ag7	0.26	**Ag21**	0.01	**Ag35**	0.38
Ag8	0.08	**Ag22**	0.17	**Ag36**	0.38
Ag9	0.21	**Ag23**	0.29	**Ag37**	0.18
Ag10	0.22	**Ag24**	0.12	**Ag38**	0.35
Ag11	0.11	**Ag25**	0.02	**Ag39**	0.15
Ag12	0.12	**Ag26**	0.15	**Ag40**	0.17
Ag13	0.20	**Ag27**	0.18	**Ag41**	0.03
Ag14	0.32	**Ag28**	0.43	**Ag42**	0.36

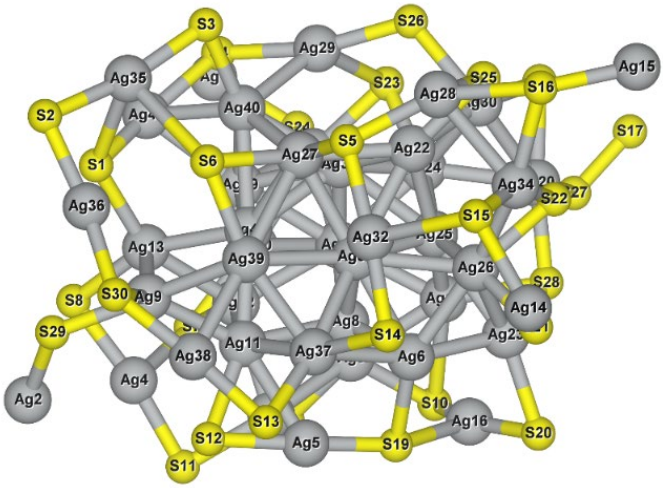

References

[1] G. Kresse, D. Joubert, *Phys. Rev. B* **1999**, *59*, 1758.

[2] G. Kresse, J. Furthmüller, *Phys. Rev. B* **1996**, *54*, 11169.

[3] J. P. Perdew, K. Burke, M. Ernzerhof, *Phys. Rev. Lett.* **1996**, *77*, 3865.

[4] J. P. Perdew, J. A. Chevary, S. H. Vosko, K. A. Jackson, M. R. Pederson, D. J. Singh, C. Fiolhais, *Phys. Rev. B* **1992**, *46*, 6671.

[5] S. Grimme, J. Antony, S. Ehrlich, H. Krieg, *J. Chem. Phys.* **2010**, *132*, 154104.

[6] J. K. Nørskov, J. Rossmeisl, A. Logadottir, L. Lindqvist, J. R. Kitchin, T. Bligaard, H. Jónsson, *J. Phys. Chem. B* **2004**, *108*, 17886.

[7] W. Tang, E. Sanville, G. Henkelman, *J. Phys. Condens. Matter* **2009**, *21*, 084204.

[8] G. Henkelman, A. Arnaldsson, H. Jónsson, *Comput. Mater. Sci.* **2006**, *36*, 354.

[9] X. Zhu, P. Zhu, X. Cong, G. Ma, Q. Tang, L. Wang, Z. Tang, *Nanoscale* **2024**, *16*, 16952.

[10] R. Wang, H. Haspel, A. Pustovarenko, A. Dikhtiarenko, A. Russkikh, G. Shterk, D. Osadchii, S. Ould-Chikh, M. Ma, W. A. Smith, K. Takanabe, F. Kapteijn, J. Gascon, *ACS Energy Lett.* **2019**, *4*, 2024.

[11] Z. Zhao, L. Lin, Y. Ni, L. Jin, L. Feng, Y. Wang, Y. Wei, J. Zhang, J. Chen, *Appl. Catal. B Environ. Energy* **2024**, *349*, 123886.

[12] M. Usman, M. H. Suliman, *Catalysts* **2023**, *13*, 867.

[13] H. Seong, K. Chang, F. Sun, S. Lee, S. M. Han, Y. Kim, C. H. Choi, Q. Tang, D. Lee, *Adv. Sci.* **2024**, *11*, 2306089.

[14] Y.-X. Wang, J. Li, F.-Q. Zhang, Z. Qi, F. Zhang, X.-M. Zhang, *ACS Cent. Sci.* **2025**, *11*, 1428.

[15] J. Zhang, T. H. M. Pham, Y. Ko, M. Li, S. Yang, C. D. Koolen, L. Zhong, W. Luo, A. Züttel, *Cell Rep. Phys. Sci.* **2022**, *3*, 100949.

[16] S. Ma, R. Luo, J. I. Gold, A. Z. Yu, B. Kim, P. J. A. Kenis, *J. Mater. Chem. A* **2016**, *4*, 8573.

[17] Y. Chen, X. Zhou, X. Liu, Z. Tang, L. Wang, Q. Tang, *J. Am. Chem. Soc.* **2025**, *147*, 2699.

[18] S. Yoo, D. Kim, G. Deng, Y. Chen, K. Lee, S. Yoo, X. Liu, Q. Tang, Y. J. Hwang, T. Hyeon, M. S. Bootharaju, *J. Am. Chem. Soc.* **2025**, *147*, 12546.

[19] G. Deng, J. Kim, M. S. Bootharaju, F. Sun, K. Lee, Q. Tang, Y. J. Hwang, T. Hyeon, *J. Am. Chem. Soc.* **2023**, *145*, 3401.

[20] C. Kim, H. S. Jeon, T. Eom, M. S. Jee, H. Kim, C. M. Friend, B. K. Min, Y. J. Hwang, *J. Am. Chem. Soc.* **2015**, *137*, 13844.

[21] L. Qin, F. Sun, X. Ma, G. Ma, Y. Tang, L. Wang, Q. Tang, R. Jin, Z. Tang, *Angew. Chem. Int. Ed.* **2021**, *60*, 26136.

[22] S. Tang, J. Xu, X. Liu, Y. Zhu, *Chem. – Eur. J.* **2022**, *28*, e202201262.

[23] N. Zhang, X. Zhang, L. Tao, P. Jiang, C. Ye, R. Lin, Z. Huang, A. Li, D. Pang, H. Yan, Y. Wang, P. Xu, S. An, Q. Zhang, L. Liu, S. Du, X. Han, D. Wang, Y. Li, *Angew. Chem. Int. Ed.* **2021**, *60*, 6170.

[24] K. Qi, Y. Zhang, J. Li, C. Charmette, M. Ramonda, X. Cui, Y. Wang, Y. Zhang, H. Wu, W. Wang, X. Zhang, D. Voiry, *ACS Nano* **2021**, *15*, 7682.

[25] Q. Lu, J. Rosen, Y. Zhou, G. S. Hutchings, Y. C. Kimmel, J. G. Chen, F. Jiao, *Nat. Commun.* **2014**, *5*, 3242.